Direct Conversion X-ray Detectors with 70 pA/cm^2 Dark Currents Coated from an Alcohol-based Perovskite Ink

Yunlong Li,[†] Emmanuel Adeagbo,[‡] Cyril Koughia,[‡] Blaine Simonson,[‡] Richard D. Pettipas,[†] Anastasiia Mishchenko,[§] Salman M. Arnab,[§] Luc Laperrière,[§] George Belev,[‖] Amy L. Stevens,[†] Safa O. Kasap,[‡] Timothy L. Kelly[†]*

[†] Department of Chemistry, University of Saskatchewan, 110 Science Place, Saskatoon, Saskatchewan, S7N 5C9, Canada

[‡] Department of Electrical and Computer Engineering, 57 Campus Drive, University of Saskatchewan, Saskatoon, Saskatchewan, S7N 5A9, Canada

[§] Analogic Canada, 4950 rue Lévy, Saint-Laurent, Québec, H4R 2P1, Canada

[‖] Saskatchewan Structural Sciences Centre, University of Saskatchewan, 110 Science Place, Saskatoon, Saskatchewan, S7N 5C9, Canada

METHODS

Physical characterization. Powder x-ray diffraction experiments were performed on a Rigaku

Ultima IV x-ray diffractometer, equipped with a Cu source (1.54056 Å), cross beam optics, and a

scintillation counter detector. The diffractometer was operated at 40 kV and 44 mA. The measurements

were carried out on the multipurpose attachment, with parallel beam mode. A parallel slit analyzer and a

K_β filter (Ni foil) were placed at the receiving end. 2θ was scanned from 10° to 65° with a step size of

0.02°. Film thicknesses were measured using a KLA-Tencor stylus surface profilometer. Scanning

electron microscope (SEM) imaging was performed using a Hitachi SU8010 microscope. UPS

measurements were collected using a Kratos (Manchester, UK) AXIS Supra system under ultrahigh

vacumn (UHV) conditions. Steady-state photoluminescence (PL) spectra were recorded on a PTI

QuantaMaster 50 fluorimeter. An excitation wavelength of 450 nm was used. Time-correlated single

photon counting (TCSPC) data were measured using a Ti:sapphire laser (Mira, Coherent) that provided

modelocked pulses in the 700−1000 nm range. The 76 MHz pulse train was sampled using a pulse

picker to provide excitation pulses at a repetition rate of 4 MHz and 500 kHz to collect short-time and

long-time data, respectively. The excitation beam was frequency doubled using a second harmonic

generator to yield 400 nm pulses.The TCSPC detection wavelengths ranged across the PL spectrum at

ca. 20 nm intervals from 760 to 820 nm. No significant difference in the lifetimes was observed at any

wavelength and the resulting TCSPC spectra were averaged.

Time of flight characterization. The TOF transient photoconductivity technique measures the

transient response due to photoinjected carriers as they drift through a sample of highly resistive

material (Figure S1). When a sample with a (semi)transparent electrode is illuminated by a pulsed light

source (from a laser), the absorbed photons generate electron-hole pairs. If the wavelength of the

excitation source is selected such that the absorption depth, δ, of the radiation is much less than the

sample thickness, L, then either holes or electrons will be immediately collected by the (semi)transparent electrode; electrons (holes) are collected for positive (negative) applied bias on this electrode. The other carrier type will drift through the sample under the influence of the applied electric field and eventually become collected by the counter electrode. The duration of the excitation must be very short compared to the transient time of the carriers to ensure that the injected carriers drift as a narrow carrier packet of charge through the sample. The number of photons must be limited so that the injected carriers do not perturb the field inside the sample. As the injected carriers drift through the sample, they induce a photocurrent, $i(t)$, through an external sampling resistor, the voltage across which is amplified and recorded on an oscilloscope.
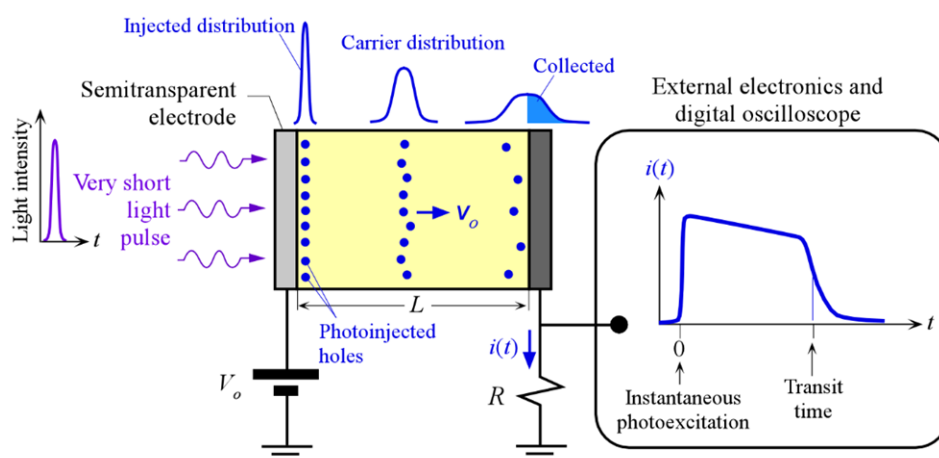

Figure S1. Principle of the time of flight (TOF) technique.

The experimental setup for the TOF measurements includes a laser, a high voltage (HV) supply, a HV triggerable electrical switch, an amplifier system with electronic protection, and a control and data acquisition system (Figure S2). A nitrogen-pumped LN103C laser is used to generate a short light pulse that is absorbed near the surface of the sample. This laser has a pulse duration of ~ 300 ps, a peak power of 250 kW, and a peak spectral output at 337.1 nm (UV) with a 0.1 nm spread. The laser pulse is then fed through a Newport optical fiber adapter and to the sample. The voltage supply is an EG&G Ortec

556 high voltage supply, which is switched onto the sample by a HV relay that is externally trigged. The transient voltage signal across R (proportional to $i(t)$) is amplified by an OPA657, 1.6-GHz, low-noise, FET-input operational amplifier, configured in a wideband, noninverting operation with a gain of +10. Its input is protected against the high voltage switching transient during the application/removal of the bias. The 8-bit Tektronix TDS210 digital oscilloscope with a sampling rate of 1 GB/s acquires the signal that comes out of the amplifier system. The oscilloscope is interfaced with the computer using a GPIB connection. A GUI user interface, realized through LabView software, was implemented on a computer. The interface allows adjustment of the oscilloscope parameters, turning on and off the high voltage switch, and allows the user to perform TOF measurements multiple times. The waveform can be saved in text.txt form on the computer. In addition, the interface provides a calculation of the drift mobility. The whole TOF experiment is computer cotrolled, which generates the trigger signals to apply the external bias, disengage the amplifier protection circuit, and trigger the laser pulse. Single shot measurements were carried out to avoid space charge build-up. The sample does not have the PMMA layer but a semitransparenet Au electrode. The applied voltage is swichted on and then off within ~1 ms and the laser is triggered within ~100 µs after the application of the pulsed bias. Typical transit times (10 – 100 ns) are much shorter than the dielectric relaxation time (~0.1 s) Due to the high dark current, the photocurrent waveforms were noisy; however, a transit time could still be discerned, as apparent in Figure 2e. The transit times followed the expected scaling with the reciprocal bias voltage (Figure 2c).
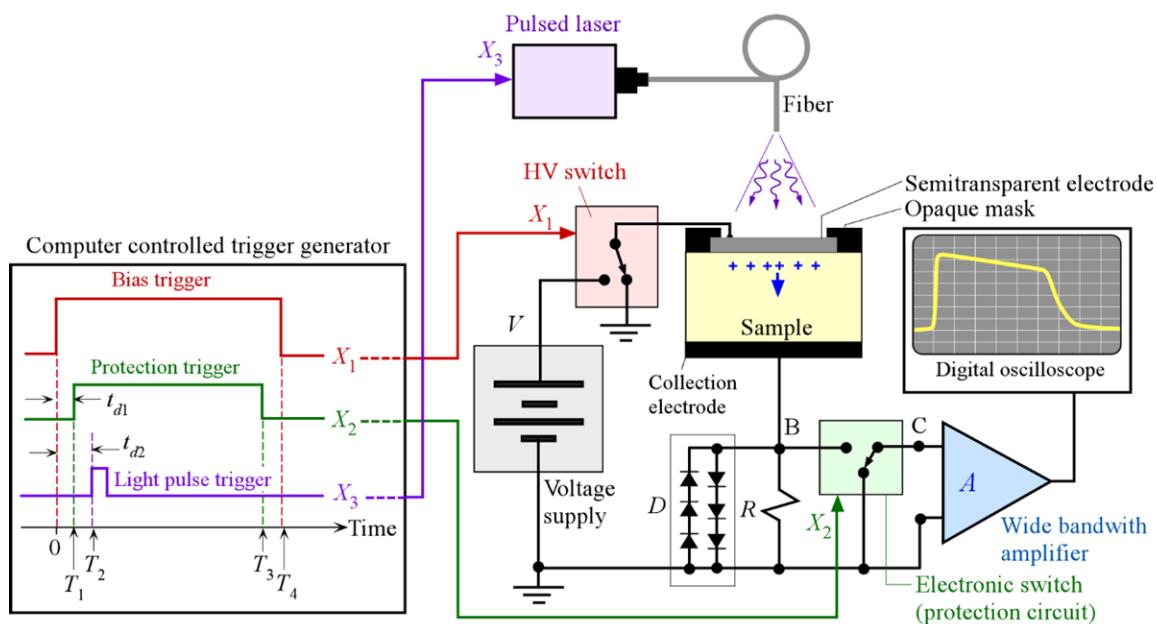
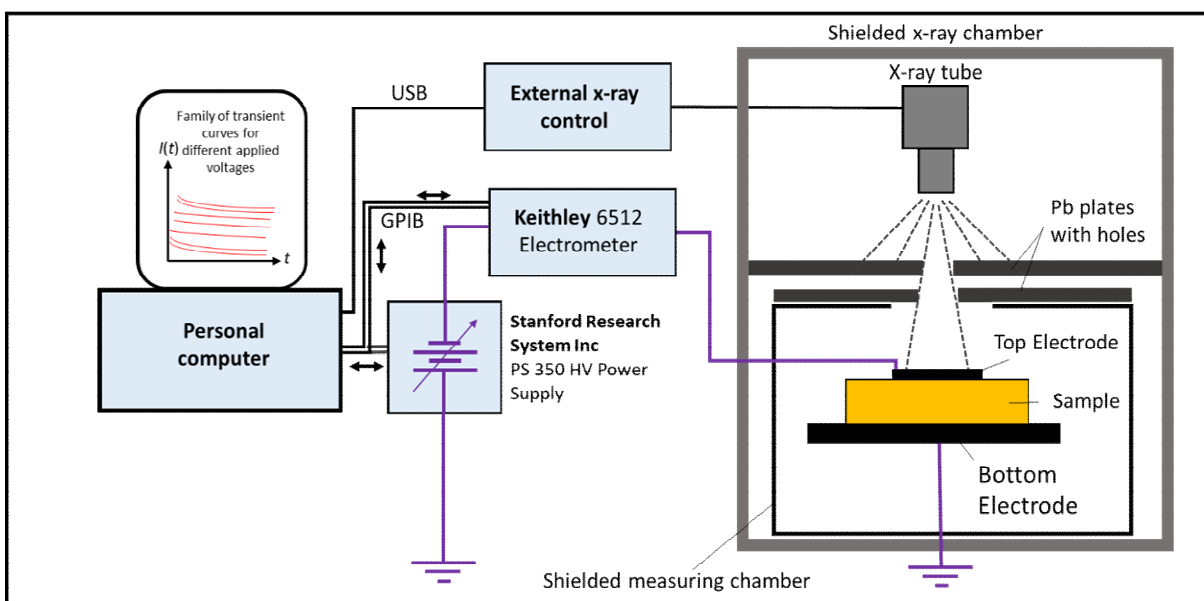**Figure S2.** A simplified schematic of the experimental TOF apparatus.

Figure S3. A simplified schematic of the X-ray characterization system.
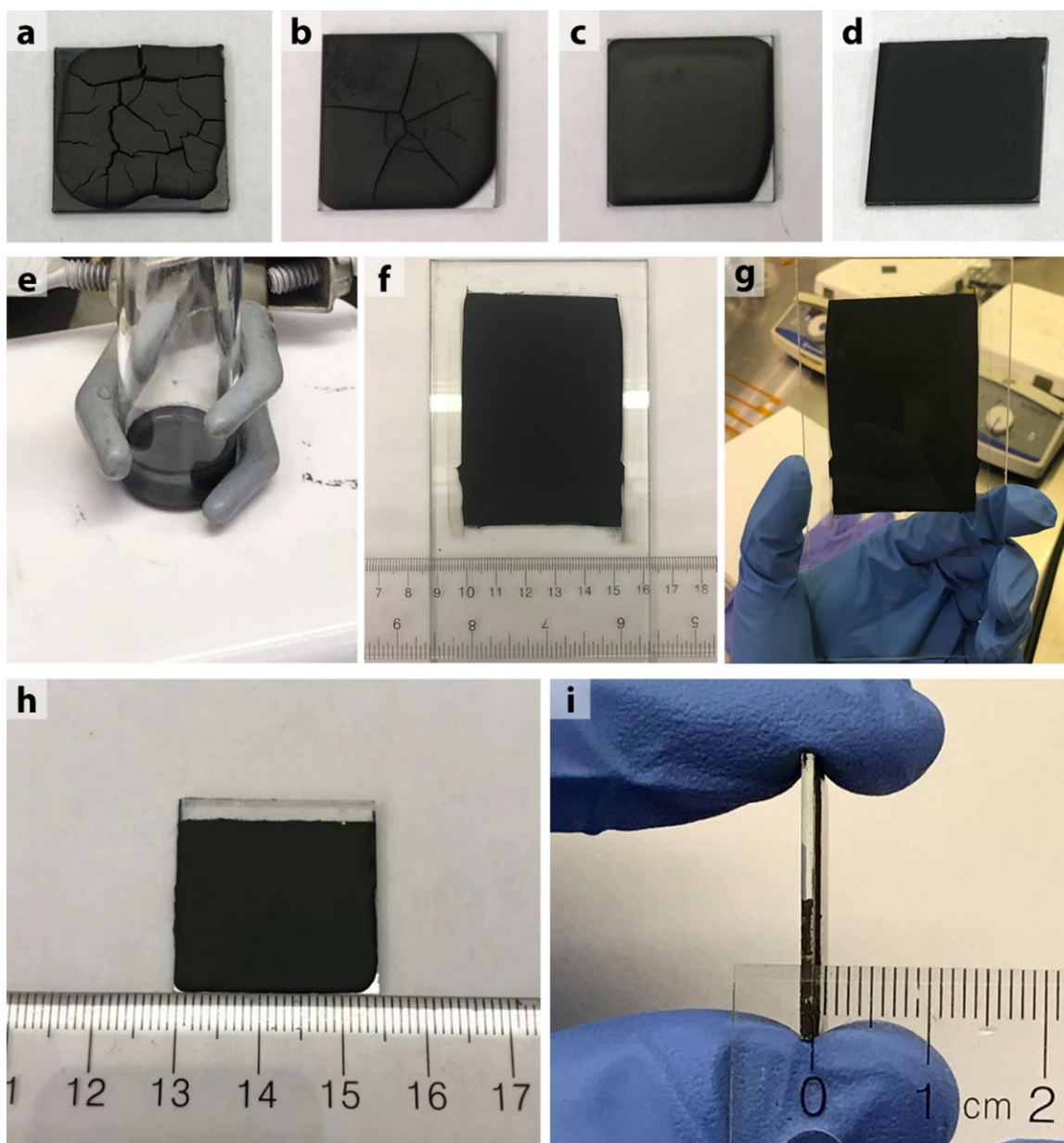
Figure S4. Photograph of pigment-based perovskite film. (a) Top view of the perovskite film based on 0% H_2O. (b) Top view of the perovskite film based on 5% H_2O. (c) Top view of the perovskite film based on 10% H_2O. (d) Top view of the perovskite film based on 15% H_2O. (e) Perovskite ink precursor based on 15% H_2O. (f) Top view of a 50 mm × 75 mm perovskite film. (g) Bottom view of a 50 mm × 75 mm perovskite film. (h) Top view of a 25 mm × 25 mm perovskite film. (i) Side view of the 500 μm-thick perovskite film.
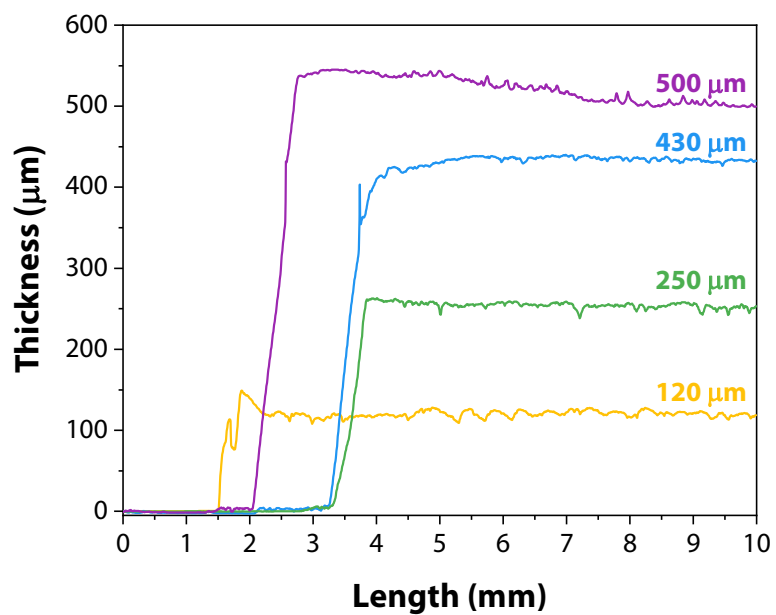
Figure S5. Profilometry data for MAPbI$_3$ films with different thickness.

TCSPC Fitting. TCSPC data were measured in two separate time regimes: $0 - 60$ ns (4 MHz repetition rate) and $0 - 2000$ ns (400 kHz repetition rate). The data at shorter time scales ($2 - 54$ ns) were fit to a biexponential decay (A_1, τ_1, A_2, τ_2) with a baseline offset (y_0):

$$y = A_1 \times \exp\left(-\frac{x}{\tau_1}\right) + A_2 \times \exp\left(-\frac{x}{\tau_2}\right) + y_0 \tag{1}$$

The data at longer time scales ($500 - 2000$ ns) were fit using a single exponential decay (τ_1) with a baseline offset (y_0):

$$y = \exp\left(-\frac{x}{\tau_1}\right) + y_0 \tag{2}$$

Table S1. TCSPC fitting parameters.

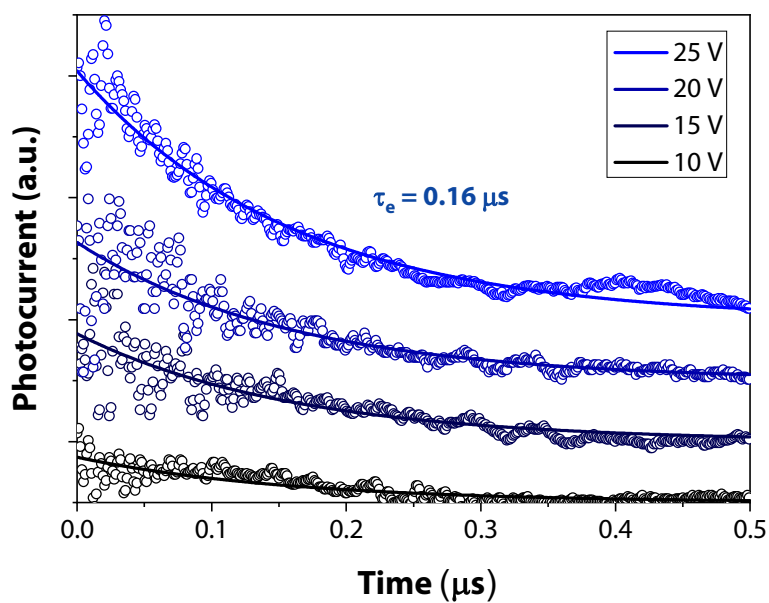| Time Scale	A_1	τ_1 (ns)	A_2	τ_2 (ns)	y_0
$2 - 54$ ns	0.925	1.09 ± 0.02	0.075	9.6 ± 0.2	0.0238 ± 0.0002
$500 - 2000$ ns	N/A	394 ± 7	N/A	N/A	$(8.5 \pm 0.1) \times 10^{-4}$

Figure S6. TOF characterization of electrons. TOF transient electron photocurrents (open circles) and the corresponding fits (solid lines).
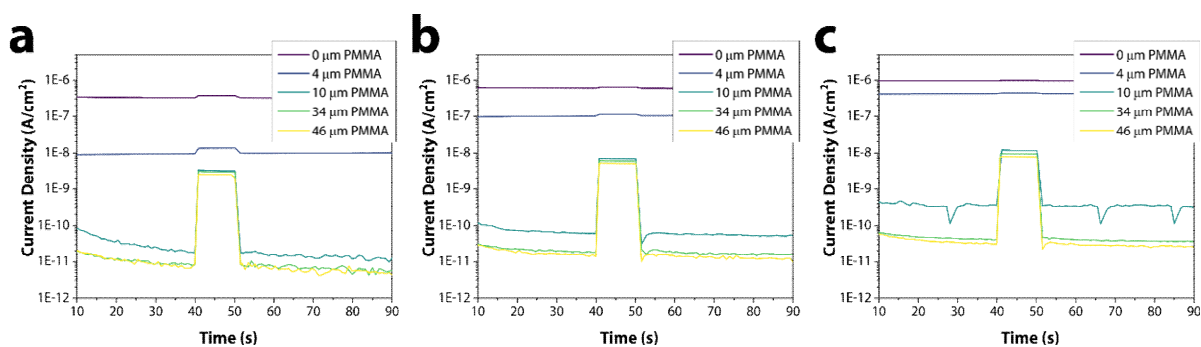

Figure S7. Effect of PMMA thickness on the detector response to 20 kV_p x-ray exposure. (a) 100 V applied bias. (b) 250 V applied bias. (c) 500 V applied bias.
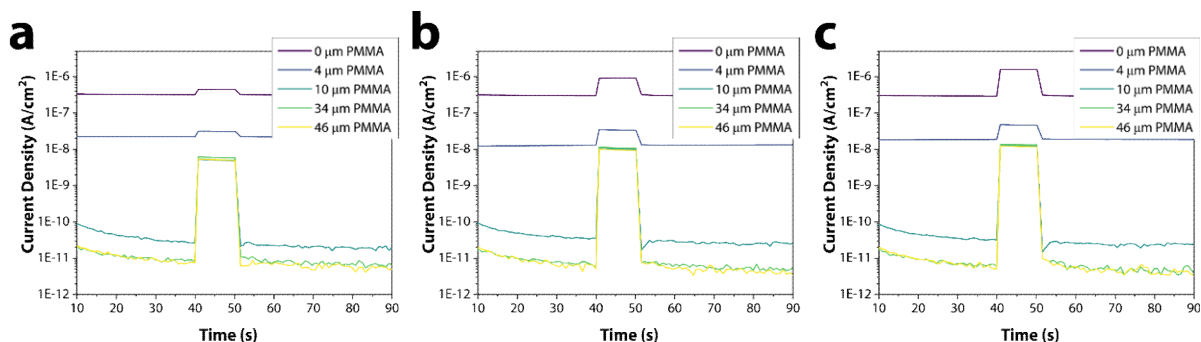
Figure S8. Effect of PMMA thickness on the detector response at 100 V applied bias. (a) 30 kV$_p$ x-ray exposure. (b) 70 kV$_p$ x-ray exposure. (c) 100 kV$_p$ x-ray exposure.
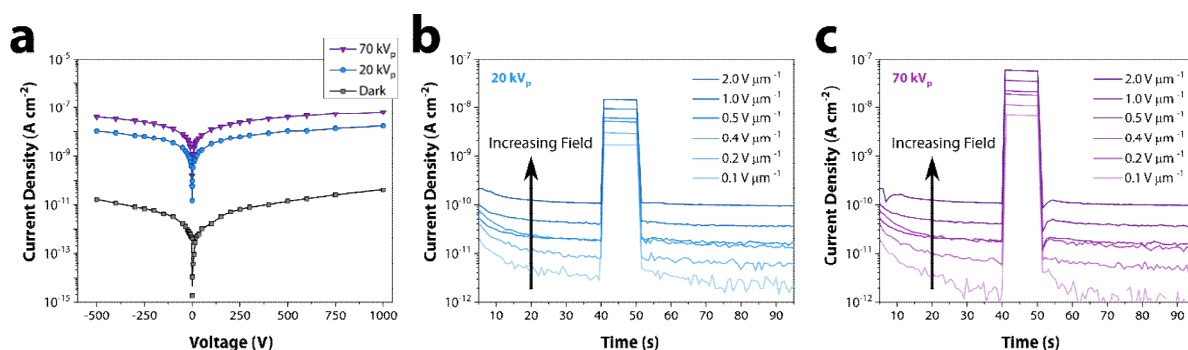

Figure S9. X-ray responses of the optimized perovskite detector. (a) *J-V* curves of the MAPbI$_3$-based x-ray detector in the dark (gray squares) and while exposed to either 20 kV$_p$ (blue circles) or 70 kV$_p$ (purple triangles) x-rays. (b) Current density traces showing the detector response to a 20 kV$_p$ x-ray pulse at various electric fields. (c) Current density traces showing the detector response to a 70 kV$_p$ x-ray pulse at various electric fields.

Time-resolved model. Consider the response function $f(t)$ that represents the decay of the photocurrent in a perovskite sample after a delta function excitation, where t is time after the cessation of excitation. In this case, the reaction to the time dependent excitation, $G(t)$, may be calculated as:

$$R(t) \propto \int_0^t G(t')f(t-t')dt' \tag{3}$$

Figure 3f and Figure S10 compare the experimentally-observed x-ray photocurrent in the MAPbI$_3$ device under half-rectified sinusoidal excitation:

$$G(t) \propto \sin(2\pi\upsilon t) \tag{4}$$

with model predictions using a system response function $f(t)$ given as:

$$f(t) = \exp\left[-\left(\frac{t}{\tau}\right)^\gamma\right] \tag{5}$$

where τ and γ are adjustable constants. The stretched exponential provides for a distribution of time constants that may be involved in generating the response; τ in (5) is some mean time constant and γ represents the distribution of time constants ($\gamma = 1$ corresponds to a system with a single time constant). From fitting the experimental curves with (3) in which $f(t)$ is described by (5), we find $\tau = 0.03$ ms while γ varies from 0.25 (for excitation at 20 kV$_p$) to 0.28 (for 100 kV$_p$). Knowledge of the response function $f(t)$ allows us to predict how fast the photocurrent decay is after cessation of x-ray excitation, as shown in Figure S11.
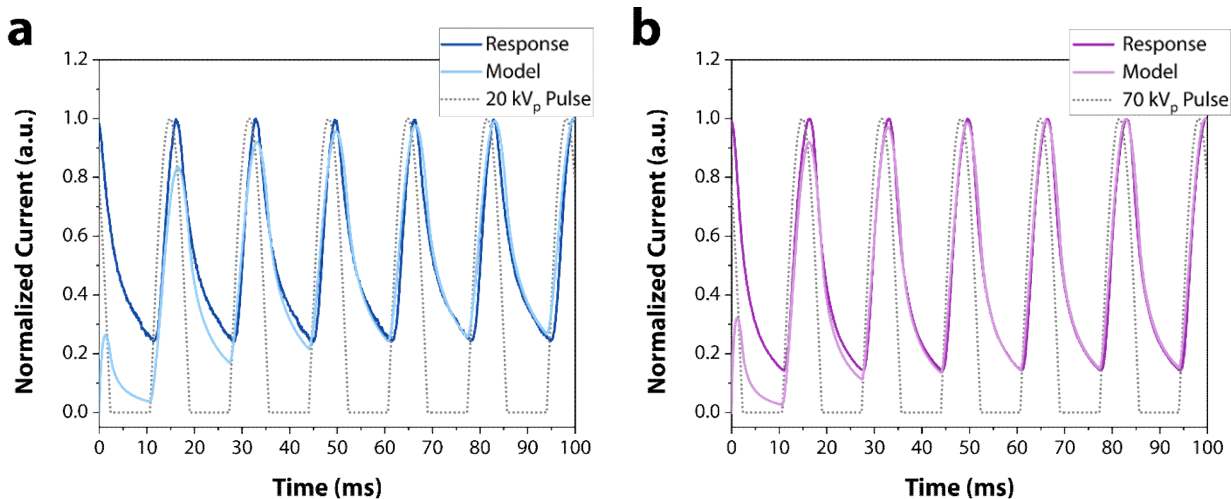
Figure S10. Response time of the MAPbI$_3$-based detector. (a) Current trace showing the detector response to a 20 kV$_p$ x-ray pulse train. (b) Current trace showing the detector response to a 70 kV$_p$ x-ray pulse train. Both pulse trains are derived from a 60 Hz half-rectified source.
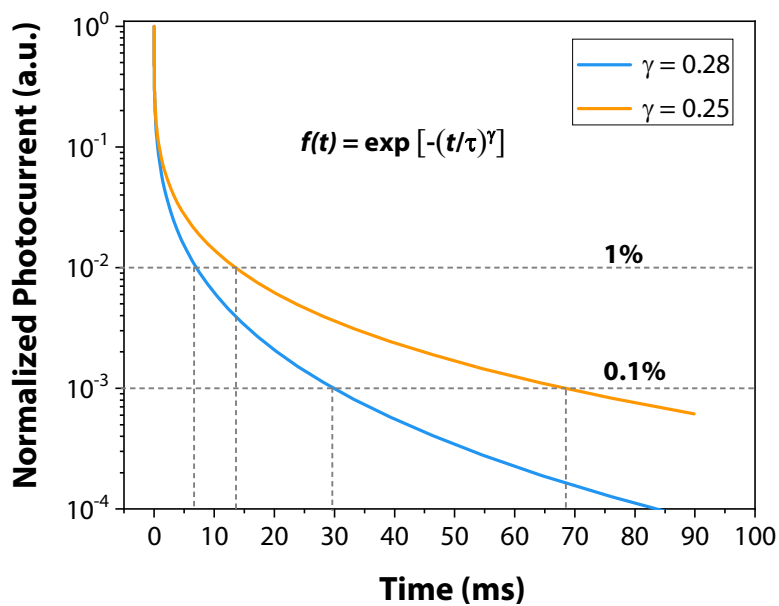

Figure S11. Response function *f*(*t*) of the MAPbI$_3$-based x-ray detector.
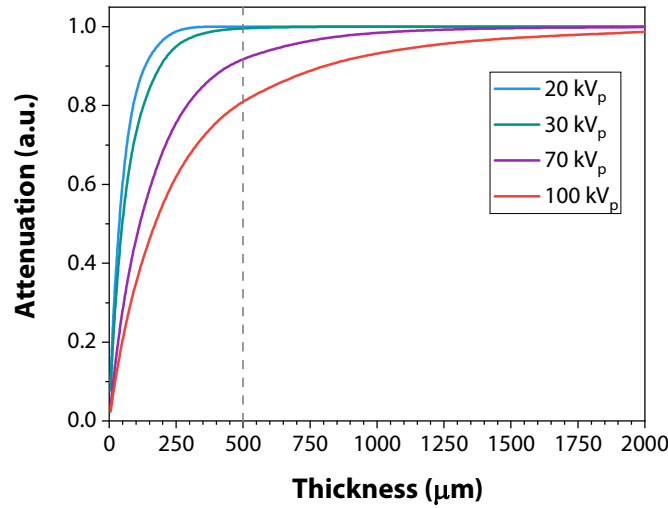
Figure S12. Calculated x-ray attenuation by MAPbI$_3$ as a function of film thickness for various peak voltages.

Limit of Detection (LoD). The limit of detection is determined by the signal (current density) that is equal to three times the background noise of the measurement (standard deviation of the dark current density), and by the x-ray sensitivity (S_x):

$$\text{LoD} = \frac{J_{\text{dark}} + 3\sigma_{\text{dark}}}{S_x} \tag{6}$$

When the dark current can be zeroed prior to measurement, $J_{\text{dark}} = 0$, and:

$$\text{LoD} = \frac{3\sigma_{\text{dark}}}{S_x} \tag{7}$$

Here we estimate σ_{dark} as 2.6×10^{-11} A/cm^2 (Figure S13); note that this represents the noise of the entire measurement system, and the true noise of the detector may be lower. At 30 kV$_p$, $S_x = 22$ µC Gy$_{\text{air}}^{-1}$ cm^{-2} (Figure 4d), and we calculate a LoD of 3.5 µGy$_{\text{air}}$ s^{-1}. In comparison, we estimate σ_{dark} as 2.5×10^{-11} A/cm^2 for *a*-Se, and with $S_x = 20$ µC Gy$_{\text{air}}^{-1}$ cm^{-2} at 30 kV$_p$, we calculate a LoD of 3.8 µGy$_{\text{air}}$ s^{-1}.
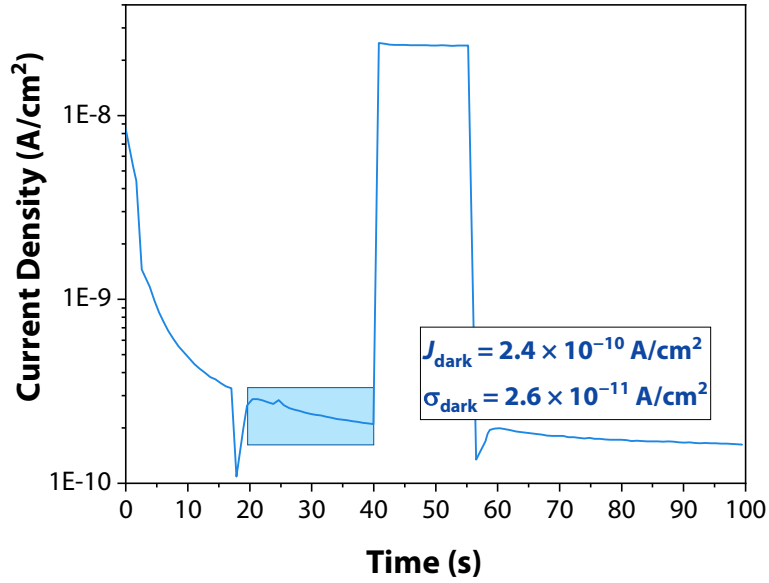
Figure S13. Current density (E = 4 V/μm) as a function of time for a MAPbI$_3$ device before, during, and after x-ray exposure. The average dark current density (J_{dark}) and the standard deviation in the dark current density (σ_{dark}) are determined from the 20 s immediately preceding the x-ray pulse (shaded blue box).

We can determine a specific detectivity, D^*, for x-ray detectors in a manner analogous to that used for photodiodes in standard optoelectronics.[1] We first calculate the noise equivalent power (NEP), which is an optoelectronic metric used to compare photodiode performance; the NEP is the input power (P_1) required to generate an output signal equal to the noise arising from the photocurrent (I_{ph}) and the dark current (I_{dark}), per square root of bandwidth (B). Assuming that the noise arises primarily from shot noise of the detector in the dark under sufficiently small signals, the NEP is given by:

$$\text{NEP} = \frac{P_1}{\sqrt{B}} = \frac{1}{R}\sqrt{2eI_{dark}} \tag{8}$$

where, R is the responsivity, which is defined as the output current (I_{ph}) per unit incident radiation power (P).

$$R = \frac{I_{ph}}{P} \tag{9}$$

Our device has a cross-sectional area A and the incident dose rate $\dot{D}$ is in $\mathrm{Gy_{air}}\ \mathrm{s}^{-1}$. The conversion of incident dose D to incident energy fluence Ψ_E (incident radiation energy per unit area) is straightforward and given by:[2]

$$\Psi_E = D\left(\frac{\rho_{\mathrm{air}}}{\mu_{\mathrm{en,air}}}\right) \tag{10}$$

where $\mu_{\mathrm{en,air}}/\rho_{\mathrm{air}}$ is the mass energy-absorption coefficient of air. The device has an area A so that the incident energy is $A\Psi_E$. If $\dot{D}$ is the dose rate, the incident radiation power is therefore:

$$P = \left(\frac{\rho_{\mathrm{air}}}{\mu_{\mathrm{en,air}}}\right) A\dot{D} \tag{11}$$

We can substitute (11) into (9) and then use the definition of x-ray sensitivity S_x (x-ray photocurrent density per unit dose rate in air), to relate R and S_x:

$$R = S_x\left(\frac{\mu_{\mathrm{en,air}}}{\rho_{\mathrm{air}}}\right) \tag{12}$$

Substituting this into (8), we obtain the NEP as a function of both S_x and I_{dark}

$$\mathrm{NEP} = \frac{1}{S_x\left(\frac{\mu_{\mathrm{en,air}}}{\rho_{\mathrm{air}}}\right)}\sqrt{2eI_{\mathrm{dark}}} \tag{13}$$

and since I_{dark} is simply the dark current density (J_{dark}) multiplied by the device area (A), we can equivalently write:

$$\mathrm{NEP} = \frac{1}{S_x\left(\frac{\mu_{\mathrm{en,air}}}{\rho_{\mathrm{air}}}\right)}\sqrt{2eJ_{\mathrm{dark}}A} \tag{14}$$

Next, the detectivity (D) is defined as the inverse of the NEP; it is therefore given by (15):

$$D = \frac{1}{\mathrm{NEP}} = \frac{S_x\left(\frac{\mu_{\mathrm{en,air}}}{\rho_{\mathrm{air}}}\right)}{\sqrt{2eJ_{\mathrm{dark}}A}} \tag{15}$$

The specific detectivity D^* is defined as $D\sqrt{A}$ and given by:

$$D^* = \frac{\sqrt{A}}{\mathrm{NEP}} = \frac{S_x\left(\frac{\mu_{\mathrm{en,air}}}{\rho_{\mathrm{air}}}\right)}{\sqrt{2eJ_{\mathrm{dark}}}} \tag{16}$$

$D*$ has units of m Hz$^{1/2}$ W^{-1}, or more commonly, cm Hz$^{1/2}$ W^{-1} (Jones).

The energy absorption coefficient of air is strongly temperature dependent and the above equation is for a single photon energy (an "effective photon energy"). One can estimate $D*$ by taking the reported peak voltage (kV$_p$) and setting the effective photon energy to one-half the peak voltage. Specific detectivities estimated using this approach are reported in Table S2.

A more rigorous approach would consider the DQE (detective quantum efficiency), which would consider the quantum noise in the radiation, conversion variance from photons to charges (the Fano factor), charge collection variance (due to incomplete charge collection) and the noise in the dark current, rather than simply the dark current alone.

Table S2. Figures-of-merit for literature benchmarks.

Material	Sensitivity ($\mu C\ Gy_{air}^{-1}\ cm^{-2}$)	J_{dark} (nA cm^{-2})	Limit of Detection ($\mu Gy_{air}\ s^{-1}$)	Specific Detectivity[a] (cm Hz$^{1/2}$ W^{-1})	Ref.
MAPbI$_3$/PMMA	22 (4 V/μm, 30 kV$_p$)	0.24 (4 V/μm)	3.5[b]	2.9×10^9 (4 V/μm, 30 kV$_p$)	This work
a-Se	20 (10 V/μm, 30 kV$_p$)	0.04 (10 V/μm)	3.8[b]	6.2×10^9 (10 V/μm, 30 kV$_p$)	This work
MAPbI$_3$ (thin film)	1.5 (0 V/μm, 75 kV$_p$)	N/A	N/A	N/A	3
MAPbI$_3$ (wafer)	2527 (0.2 V/μm, 70 kV$_p$)	6000 (0.2 V/μm)	N/A	23×10^9 (0.2 V/μm, 70 kV$_p$)	4
MAPbI$_3$ (polycrystalline)	11000 (0.24 V/μm, 100 kV$_p$)	250[d] (0.24 V/μm)	N/A	45×10^9 (0.24 V/μm, 100 kV$_p$)	5
MAPbBr$_3$ (single crystal)	80 (5×10^{-5} V/μm, 50 kV$_p$)	29 (5×10^{-5} V/μm)	0.5[c]	2.0×10^9 (5×10^{-5} V/μm, 50 kV$_p$)	6
MAPbBr$_3$ (single crystal)	322 (5×10^{-4} V/μm, 50 keV)	23 (5×10^{-4} V/μm)	0.036[c]	7.9×10^9 (5×10^{-4} V/μm, 50 keV)	7
MAPbI$_3$ (single crystal)	968.9 (0.001 V/μm, 50 kV$_p$)	3000[d] (0.001 V/μm)	N/A	24×10^9 (0.001 V/μm, 50 kV$_p$)	8
Cs$_2$AgBiBr$_6$ (single crystal)	25[d] (0.0025 V/μm, 50 kV$_p$)	0.15 (0.0025 V/μm)	0.0597[c]	0.6×10^9 (0.0025 V/μm, 50 kV$_p$)	9

[a] calculated using Equation 18 and μ_{en}/ρ values for air, interpolated from tabulated data[10] and assuming $E = \frac{1}{2}$ kV$_p$; [b] estimated from Equation 7; [c] as-reported; [d] estimated from figures in the paper.
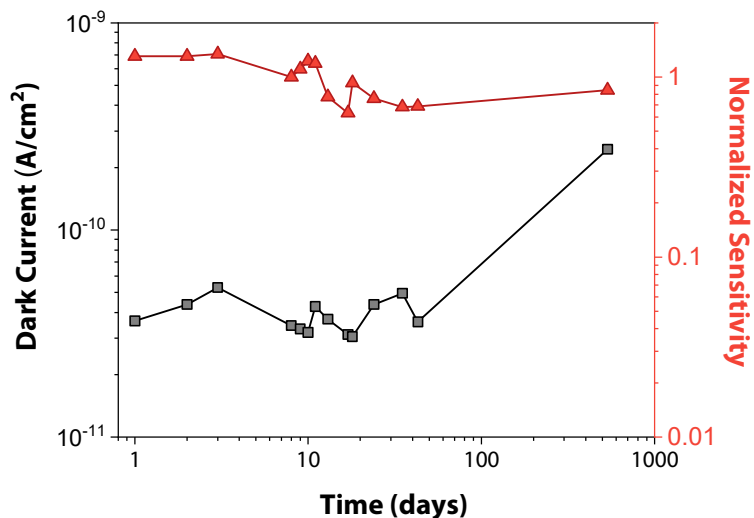
Figure S14. Shelf-life measurements. Measurements of dark current density ($E = 2$ V/μm) and normalized x-ray sensitivity (20 kV$_p$ x-rays, $E = 2$ V/μm) for MAPbI$_3$ devices as a function of device storage time in air.
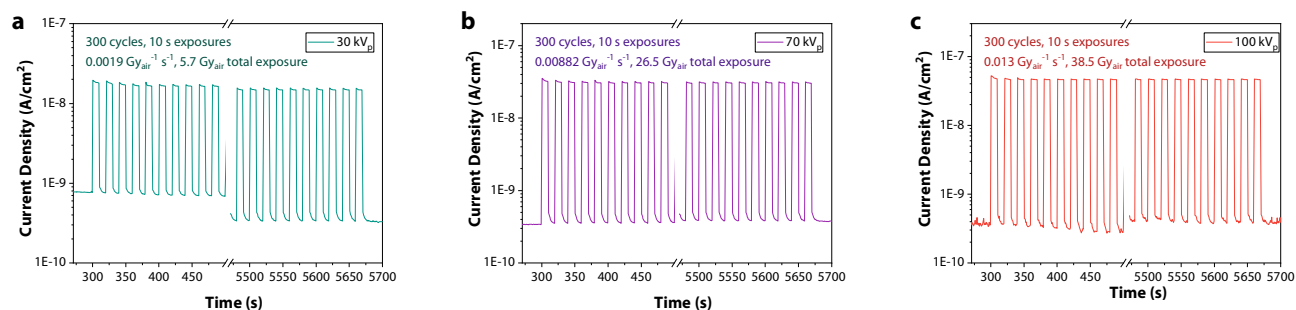

Figure S15. Device stability under operational conditions. Current response of the MAPbI$_3$-based device upon repeated cycling in air. **a,** 30 kV$_p$. **b,** 70 kV$_p$. **c,** 100 kV$_p$.
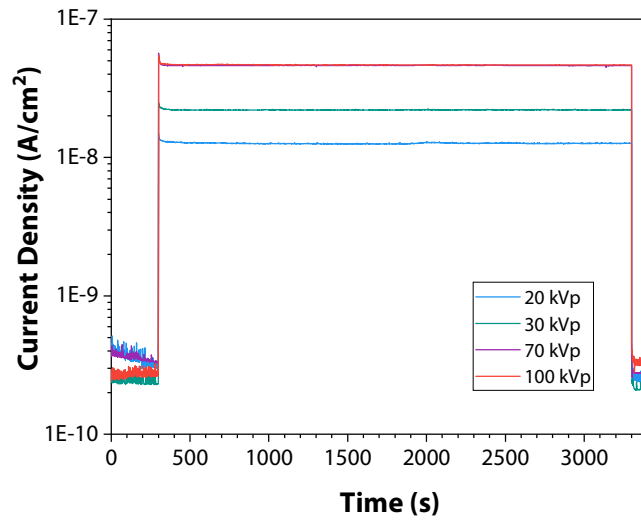
Figure S16. Device stability under operational conditions. Current response of the MAPbI$_3$-based device upon extended x-ray exposure in air ($E = 2$ V/μm).
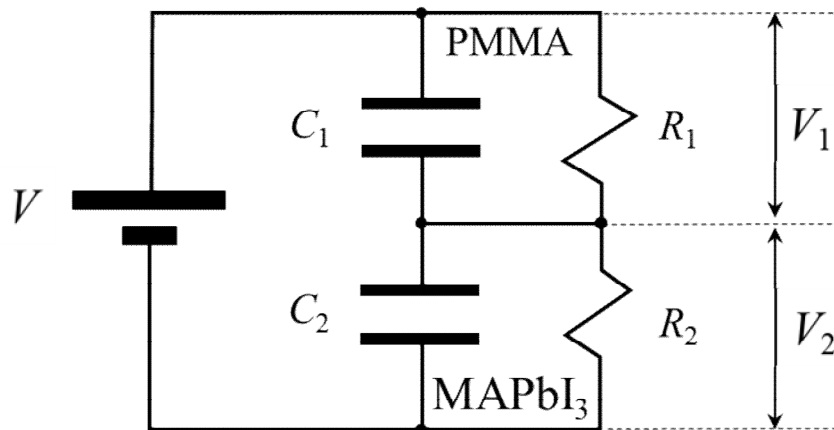

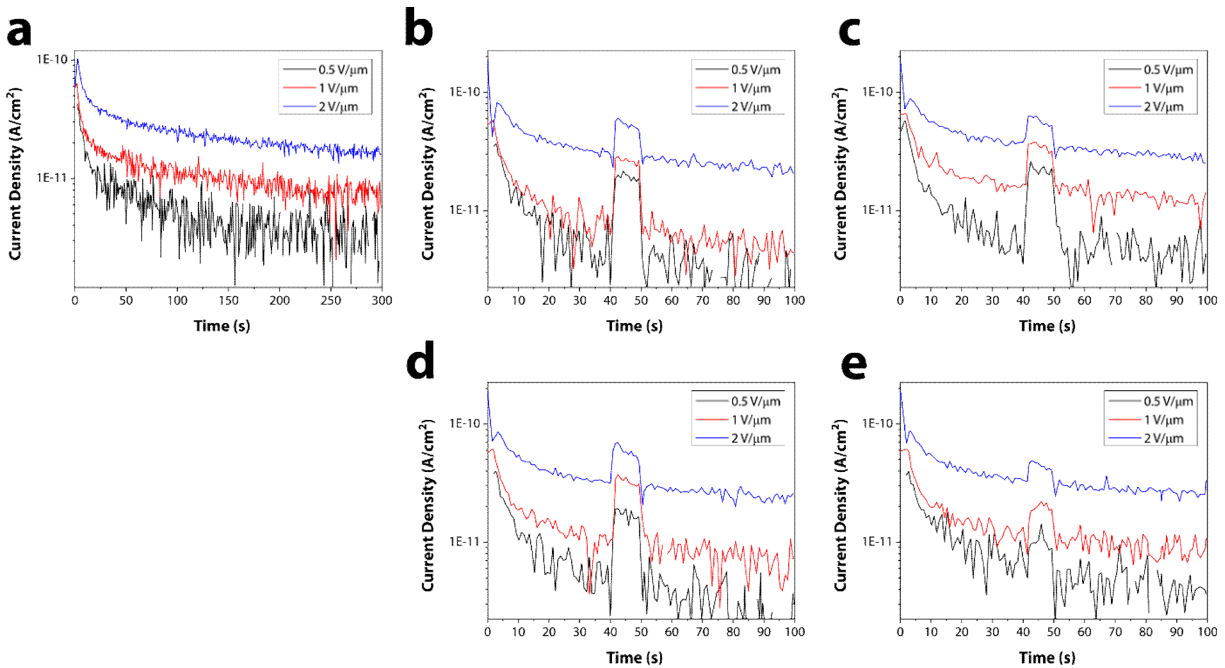**Figure S17.** Equivalent *RC*-circuit model of the MAPbI$_3$/PMMA structure.

Figure S18. Current density as a function of time for ITO/PMMA/Al devices, before, during, and after an x-ray pulse: (a) dark, no x-ray; (b) 20 kV$_p$; (c) 30 kV$_p$; (d) 70 kV$_p$; (e) 100 kV$_p$.

REFERENCES

1.   Kasap, S. O. *Optoelectronics and Photonics: Principles and Practices*. (Pearson, 2013).

2.   Johns, H. E. & Cunningham, J. R. *The Physics of Radiology*. (Charles C. Thomas, 1983).

3.   Yakunin, S. *et al.* Detection of X-ray photons by solution-processed lead halide perovskites. *Nat. Photonics* **9**, 444–449 (2015).

4.   Shrestha, S. *et al.* High-performance direct conversion X-ray detectors based on sintered hybrid lead triiodide perovskite wafers. *Nat. Photonics* **11**, 436–440 (2017).

5.   Kim, Y. C. *et al.* Printable organometallic perovskite enables large-area, low-dose X-ray imaging. *Nature* **550**, 87–91 (2017).

6.   Wei, H. *et al.* Sensitive X-ray detectors made of methylammonium lead tribromide perovskite single crystals. *Nat. Photonics* **10**, 333–339 (2016).

7.   Wei, W. *et al.* Monolithic integration of hybrid perovskite single crystals with heterogenous

substrate for highly sensitive X-ray imaging. *Nat. Photonics* **11**, 315–321 (2017).

8.   Ye, F. *et al.* High-Quality Cuboid CH3NH3PbI3 Single Crystals for High Performance X-Ray and Photon Detectors. *Adv. Funct. Mater.* **29**, 1–7 (2019).

9.   Pan, W. *et al.* Cs2AgBiBr6 single-crystal X-ray detectors with a low detection limit. *Nat. Photonics* **11**, 1–8 (2017).

10.   Hubbell, J. H. & Seltzer, S. M. *Tables of X-Ray Mass Attenuation Coefficients and Mass Energy-Absorption Coefficients from 1 keV to 20 MeV for Elements Z = 1 to 92 and 48 Additional Substances of Dosimetric Interest*. *NIST Standard Reference Database 126* (National Institute of Standards and Technology).